

Steam Reforming of Methane Over Nickel: Development of a Multi-Step Surface Reaction Mechanism

*L. Maier, B. Schädel, K. Herrera Delgado,
S. Tischer & O. Deutschmann*

Topics in Catalysis

ISSN 1022-5528

Volume 54

Combined 13-15

Top Catal (2011) 54:845-858

DOI 10.1007/s11244-011-9702-1

Your article is protected by copyright and all rights are held exclusively by Springer Science+Business Media, LLC. This e-offprint is for personal use only and shall not be self-archived in electronic repositories. If you wish to self-archive your work, please use the accepted author's version for posting to your own website or your institution's repository. You may further deposit the accepted author's version on a funder's repository at a funder's request, provided it is not made publicly available until 12 months after publication.

Steam Reforming of Methane Over Nickel: Development of a Multi-Step Surface Reaction Mechanism

L. Maier · B. Schädel · K. Herrera Delgado ·
S. Tischer · O. Deutschmann

Published online: 2 August 2011
© Springer Science+Business Media, LLC 2011

Abstract A detailed multi-step reaction mechanism is developed for modeling steam reforming of methane over nickel-based catalysts. The mechanism also includes partial and total oxidation reactions, water–gas shift reactions, formation of carbon monolayers, and methanation reactions. A method is presented for ensuring thermodynamic consistency in the development of surface reaction mechanisms. The applicability of the mechanism is tested by simulating experimental investigations of SR of methane on a Ni-coated monolithic cordierite catalyst as well as experimental studies from literature. The reactive flow in the channels of the experimentally used monolithic structures is modeled by a two-dimensional flow field analysis of a single monolith channel coupled with the reaction mechanism developed. The gas composition and surface coverage with adsorbed species are calculated as function of the position in the channel. The model developed is able to properly describe steam reforming of methane over the nickel catalysts for wide ranges of temperature and steam/methane ratio.

Keywords Catalysis · Reforming · Methane · Synthesis gas · Surface reaction mechanism · Nickel · Numerical simulation

1 Introduction

Synthesis gas (H_2/CO in various compositions) plays a key role as a feedstock in many catalytic processes such as synthesis of methanol, oxo-synthesis, and Fischer–Tropsch synthesis. Hydrogen as a separate component of synthesis gas is largely used in the manufacturing of ammonia, in a variety of petroleum hydrogenation processes, and as a clean fuel for burners or fuel cells. Steam reforming of methane (natural gas) has been the most widely used industrial process, because it is one of the most efficient technologies for hydrogen and the synthesis gas production from fossil fuels in large scale facilities reaching yields close to the thermodynamic equilibrium [1, 2]. Steam reforming is a highly endothermic reaction and requires an efficient external energy supply, disadvantageous in small scale operation units. Conventional steam reformers deliver relatively high concentrations of hydrogen at high fuel conversion [3]. The molar steam/carbon (S/C) ratio usually exceeds 2.5. The excess steam supports completion of the reaction and inhibits coke formation, however, additional heat must be added [4, 5]. The products of the reaction are controlled mainly by thermodynamics, which favor the formation of methane at lower temperatures and of hydrogen at higher ones. Recently, direct synthesis of Ni based hydrotalcite was used to prepare small Ni nanocrystals, which can efficiently be applied for sorption enhanced steam methane reforming [6].

In recent years, (catalytic) partial oxidation ((C)POX) [7–12], in particular over noble metal catalysts and at short contact times, as well as CO_2 reforming [13–15] of natural gas to synthesis gas have also attracted much interest because of their potential to reduce the cost of synthesis gas production and environmental concerns, respectively. POX and autothermal reforming (ATR)—a combination of SR

L. Maier · O. Deutschmann
Institute for Catalysis Research and Technology, Karlsruhe
Institute of Technology (KIT), 76128 Karlsruhe, Germany

B. Schädel · K. Herrera Delgado · S. Tischer ·
O. Deutschmann (✉)
Institute for Chemical Technology and Polymer Chemistry,
Karlsruhe Institute of Technology (KIT), 76128 Karlsruhe,
Germany
e-mail: deutschmann@kit.edu

and POX—do not require external energy supplies. Dry reforming (DR) using CO_2 is especially discussed in the light of the useful processing of a greenhouse gas in the chemical industry. The energy and steam produced by the exothermic oxidation reactions in ATR and POX sustain the endothermic reforming reactions to autothermally operate the reactor [16].

For reaching a profound understanding of the reaction mechanism of synthesis gas formation from methane by SR and POX, the sequence and interaction of the reaction routes have to be analyzed for the combined POX–SR–DR systems, because the conditions in any flow reactor vary along the flow directions, covering a wide range of mixture compositions and leading to quite different local reaction rates. In CPOX over the commonly used Rh catalysts, the general consensus is now that the overall conversion is realized in a two-step process (indirect route), in which first CH_4 is totally oxidized to CO_2 and steam, as long as oxygen is present close to the catalyst surface, and then the remaining CH_4 is reformed with steam and (or) CO_2 to synthesis gas [7–9, 17]. A decade ago, a direct CPOX route had also been considered [10–12]. Detailed reaction schemes for the catalytic partial oxidation of methane over platinum and rhodium, which also include steps for steam reforming, were published by Schmidt et al. [10, 18], Vlachos et al. [19], and Deutschmann et al. [17, 20, 21]. The development of a detailed mechanism for simultaneous modeling of partial oxidation and steam reforming over nickel catalysts has not been described yet, even though reaction kinetics of methane steam reforming over nickel catalysts has been extensively investigated experimentally and theoretically [22–28]. A review on catalytic partial oxidation of methane to synthesis gas with emphasis on reaction mechanisms over transition metal catalysts was recently published by Holmen and co-workers [29]. In most of these studies macrokinetic models were developed to describe the kinetic behavior observed.

In a pioneering study, Xu and Froment [22] described steam reforming of methane accompanied by water–gas shift reactions on a Ni/MgAl₂O₄ catalyst by intrinsic rate equations derived from a Langmuir–Hinshelwood mechanism, which is widely used in SR modeling. In a more recent study, Wei and Iglesia [30] postulated a catalytic sequence for reactions of CH_4 with CO_2 and H_2O on Ni/MgO catalysts, which could be confirmed by independent kinetic and isotopic measurements revealing the intrinsic kinetic and mechanistic equivalence among these reactions. Isotopic tracer and exchange studies provided rigorous evidence for the sole kinetic relevance of C–H bond activation steps supporting the experimental observation that CH_4 reaction rates were unaffected by the identity or concentration of co-reactants. Their isotopic studies also showed that activation of H_2 , CO_2 , and H_2O was reversible

and quasi-equilibrated in SR and DR of methane. A microkinetic model for steam reforming reactions over a Ni/MgO–MgAl₂O₄ catalyst was proposed by Apparicio [31], which was constructed on rate constants extracted from transient isotopic studies by fitting the models to response curves measured. This reaction mechanism was extended by Chen et al. [23] by reactions for CO_2 reforming of methane and deactivation by carbon formation. A hierarchical multiscale modeling approach was demonstrated in a recent work of these authors [32]. A microkinetic model for steam methane reforming on the supported Ni catalyst including reaction steps of surface carbon formation, segregation, diffusion, and precipitation was developed. Furthermore, experimental studies in a tapered element oscillating microbalance (TEOM) reactor at industrially relevant conditions were used for model evaluation.

Wang et al. [33] investigated reaction pathways of CO_2 reforming of CH_4 on Ni(111) by using density functional theory calculations. They proposed a surface reaction mechanism with CH_4 dissociative adsorption as rate-determining step and HCO as key intermediate surface adsorbed species [33]. In a their further study, these authors included the analysis of electronic energies along possible reforming pathways as well as the identification of some activation barriers but have not yet developed a complete kinetic scheme [34]. In a very interesting study, Blaylock et al. analyzed the reaction pathways and most abundant reaction intermediates on the catalyst surface in steam reforming of methane over Ni(111) using plane wave density functional theory in combination with a statistical thermodynamic treatment [35]. The authors proposed a detailed kinetic model containing adsorbed HCO and CHOH species as the most important intermediates. Application of the model for simulation of a real steam reformer has not been discussed in that paper [35]. All these kinetic models were suggested for steam—or CO_2 —reforming in the absence of oxygen in the gas phase.

In this paper, we present the development of a multi-step, thermodynamically consistent heterogeneous reaction mechanism for SR, POX, and DR of methane over Ni-based catalysts, focusing in the current paper on SR only. However, the mechanism includes adsorption, desorption, and reactions of oxygen, in order to be potentially extended for application in the partial and total oxidation regime. Also adsorption and decomposition of CO_2 is already included for potential application of the mechanism for DR investigations. The mechanism is tested by its comparison with experimentally derived data for steam reforming of methane over nickel/alumina monoliths in the temperature interval of 900–1350 K and with experimental data from literature. The mechanism here developed for Ni/alumina catalysts has also been successfully applied in numerical simulation of internal steam and DR of methane

over Ni/YSZ anodes of solid-oxide fuel cells (SOFC) at isothermal conditions of 1073 K (800 °C) [36]: In these studies thermodynamic consistency was established for 1073 K only; therefore, the actual kinetic data differ from the mechanism in Table 2. In a further study [37], the mechanism as given in Table 2 was used to numerically predict current–voltage characteristics of a SOFC button cell and species profiles within this cell over a temperature range of 873–1073 K (600–800 °C). SOFC application is beyond the scope of the present paper, which focuses on the development procedure of a detailed reaction mechanism for methane reforming over Ni/alumina and its experimental evaluation.

2 Experimental Setup

The set-up used to provide new experimental data for mechanism evaluation is described in this section, while the experimental bases for the data taken from literature are shortly described in Sect. 5. Our experiments were carried out in a flow reactor system schematically depicted in Fig. 1 [38, 39]. A liquid flow controller monitors the flow of distilled water between the pressure reservoir, storing water at 3 bars, and the vaporizer. Mass flow controllers produced by Bronkhorst Hi-Tec are used to dose the other inlet gases, argon and methane. Those gases are also fed into the vaporizer, which additionally serves as mixing-chamber.

The reactor is made out of ceramic materials (Pythagoras) and stainless steel. Three cordierite honeycomb monoliths with a diameter of 1.5 cm are placed inside the

ceramic reactor tube. The monoliths, 1 cm in length, have 89 channels with an inner hydraulic diameter of 1.13 mm. The monolith in the middle was coated with nickel by wet impregnation with an acidic aqueous solution of $\text{Ni}_2(\text{NO}_3)_2 \cdot 5\text{H}_2\text{O}$ (Alfa Aesar). After impregnation, the catalyst was dried at 400 K for 24 h, calcinated in air at 1073 K for five hours, and finally reduced for 6 h by H_2 at 773 K. This preparation procedure led to Ni loadings of approximately 3 wt%. Chemisorption measurements using hydrogen or carbon monoxide can be used to estimate the specific surface area; a ratio of active surface area to geometrical surface area of the channel wall ($F_{\text{cat}/\text{geo}}$) of 40 is used in the simulation without modification. Energy dispersive X-ray spectroscopy (EDX) measurements revealed the absence of chlorine or sulphur compounds on the catalyst surface after calcination. The catalysts do not carry a washcoat, the metal is spread on the blank cordierite surface to avoid any transport limitation within the catalyst layer.

Uncoated monoliths are placed in front and behind the catalyst. A ceramic cloth, 1 mm thick, is wound around the catalyst to prevent gas bypass. The reactor is operated isothermal at atmospheric pressure. The temperature is controlled by adjusting the furnace heating. Gas temperatures at the front and rear of the catalytic monolith are monitored with Rh/Pt-thermocouples. A third thermocouple is used to measure the temperature at the outer reactor wall. The product composition is analyzed with a gas chromatograph (Varian GC) and a quadrupole mass spectrometer (AIRSENSE 500). The mass flows of the reactants, water and methane, are varied, leading to steam/

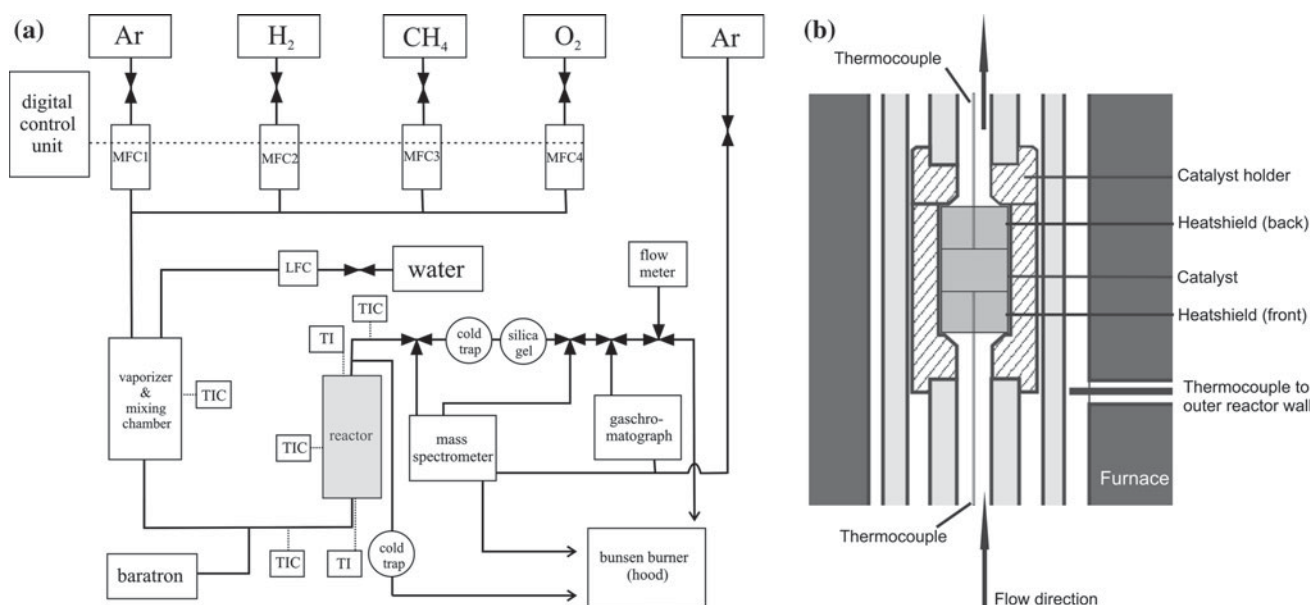


Fig. 1 Schematic of the experimental setup used for catalytic reforming experiments employing Ni-coated monoliths (a) and schematic drawing of reactor (b)

methane ratios (S/C) of one to four. Argon was used as dilution (75 vol.%), also supporting stable isothermal conditions.

For a series of measurements at constant S/C, the temperature was increased step-wise, and after the steady state was reached the exit concentration was analyzed. Potential carbon accumulation was burned off at the end of each series using 25 vol.% oxygen in argon for 30 min at 700 °C, followed by reduction with 5% hydrogen in argon for 1 h. All experiments were carried out with constant flow rates of 593 mL/min resulting in a hydraulic flow velocity in the single channels of 0.056 m/s.

3 Mathematical Model and Numerical Simulation

All experimental data used for model development were carried out in monolithic honeycomb catalysts or similar reactor configurations. Furthermore, isothermal conditions and uniform inlet flow were established. Thus, homogeneous conditions for all channels of a monolith can be assumed. Therefore it is sufficient to simulate the experiments using a single channel model.

The reactive flow field in the single catalytic channel is described by steady-state, two-dimensional boundary-layer equations with transport coefficients that depend on composition and temperature [40]. Surface reactions are modeled by a mechanism consisting of elementary-step-like reactions using the mean-field approximation [41, 42]. Along the channel, the variation of gas-phase composition in axial and radial directions as well as the axial variation of the surface coverage with adsorbed species are taken into account.

3.1 Modeling the Flow Field in a Single Channel

The rectangular shaped single channel is approximated by a cylindrical channel model. Using given inlet conditions (velocity, species mass fractions), the two-dimensional laminar, isothermal flow field of the fluid at steady state is computed using the boundary-layer approximation, which eventually leads to the following set of equations [40]:

$$\frac{\partial(r\rho u)}{\partial z} + \frac{\partial(r\rho v)}{\partial r} = 0, \tag{1}$$

$$\frac{\partial(r\rho u Y_i)}{\partial z} + \frac{\partial(r\rho v Y_i)}{\partial r} = -\frac{\partial}{\partial r}(r j_i), \tag{2}$$

$$\frac{\partial(r\rho u u)}{\partial z} + \frac{\partial(r\rho v u)}{\partial r} = -r \frac{\partial p}{\partial z} + \frac{\partial}{\partial r} \left(\mu r \frac{\partial u}{\partial r} \right). \tag{3}$$

Here, the following variables are used: z and r , axial and radial coordinates; ρ , density; u and v , axial and radial velocity components; Y_i , mass fraction; j_i , diffusive mass

flux; p , pressure. The viscosity μ and the diffusion fluxes j_i depend on temperature and species composition.

3.2 Surface Chemistry Model

The chemical source terms \dot{s}_i due to catalytic reactions are modeled by elementary-step based reaction mechanisms [42–44]. Homogeneous gas-phase reactions can be neglected under the conditions (temperature, pressure, residence time) applied in the present study. The locally varying surface coverage of adsorbed species i , Θ_i , is determined by

$$\frac{\partial \Theta_i}{\partial t} = \frac{\sigma_i \dot{s}_i}{\Gamma}, \tag{4}$$

where \dot{s}_i is the molar rate of creation or depletion of species i due to adsorption, desorption, and surface reactions, σ_i is the number of surface sites that are occupied by species i , and Γ (2.6×10^{-5} mol/m² used for Ni) is the surface site density.

The net rate of adsorption and desorption of gas-phase species is balanced by the diffusive mass flux in Eq. 2 at the surface in radial direction, $j_{i,\text{surf}}$. Convective fluxes vanish in steady-state as long as no mass is deposited or ablated. Hence, the following boundary condition applies for the flux at the inner channel wall:

$$j_{i,\text{surf}} = F_{\text{cat/geo}} \eta M_i \dot{s}_i, \tag{5}$$

where M_i is the molar mass of species i , and $F_{\text{cat/geo}}$ is the ratio between catalytic active surface area and geometric surface area. Since no washcoat is used in the present study the effectiveness factor η is unity. The total molar production rate of surface species i by heterogeneous reactions is given by

$$\dot{s}_i = \sum_{k=1}^{K_s} (v''_{ik} - v'_{ik}) k_{fk} \prod_{j=1}^{N_g+N_s} c_j^{v'_{jk}}, \tag{6}$$

where K_s is the number of surface reactions (including adsorption and desorption), v'_{ik} (reactants) and v''_{ik} (products) are the stoichiometric coefficients, and N_g and N_s are the number of gas-phase and surface species, respectively.

The temperature dependence of the rate coefficients is described by a modified Arrhenius expression:

$$k_{fk} = A_k T^{\beta_k} \exp \left[\frac{-E_{ak}}{RT} \right] \prod_{i=1}^{N_s} \exp \left[\frac{\varepsilon_{ik} \Theta_i}{RT} \right]. \tag{7}$$

This expression accounts for additional dependencies of the activation energy on coverage using the parameter ε_{ik} . The rates of adsorption reactions are calculated using sticking coefficients S^0 :

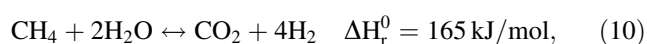
$$s_i^{\text{ads}} = S_i^0 \sqrt{\frac{RT}{2\pi M_i}} c_i^{\text{gas}} \prod_{j=1}^{N_s} \Theta_j^{v_j^k} \quad (8)$$

The computational tool DETCHEM^{CHANNEL} [43, 44] is applied to treat the problem numerically.

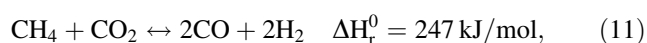
4 Chemical Reaction System

Conversion of methane and steam into a mixture of hydrogen, carbon monoxide, and carbon dioxide can be considered as a combination of the following net reactions:

endothermic steam reforming,



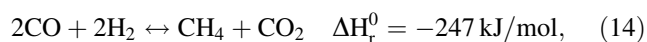
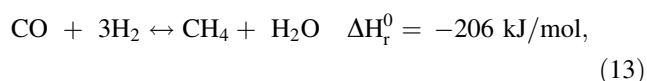
endothermic CO₂-reforming,



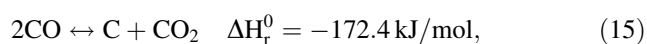
exothermic water–gas shift,



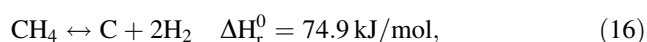
methanation,



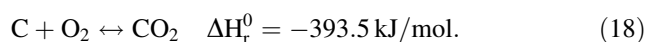
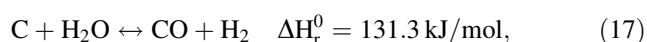
carbon formation by Boudouard reaction,



and by methane cracking,



as well as gasification of carbon by steam or oxygen,



4.1 Surface Reaction Mechanism

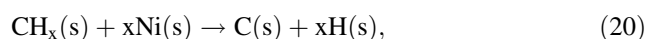
A detailed surface reaction mechanism was developed to model reforming of methane on nickel, which covers all the global reactions given above in Eqs. 9–18. The reaction mechanism consists of 42 reactions among 7 gas phase species and 14 surface species. Table 1 summarizes the reaction steps with their associated rate expressions.

The reaction mechanism suggests that adsorbed carbon species CH_x(s) (x = 0, 1, 2, 3) formed from activated methane react with adsorbed atomic oxygen O(s), formed from the adsorption of oxygen or from the decomposition

of water and CO₂, and produce carbon oxide. The total reforming process on Ni catalyst is described as follows:

Adsorption–desorption of reactants and products (R1–R12).

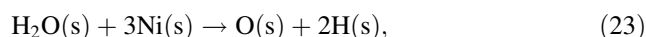
Activation of methane without oxygen (R13–R20).



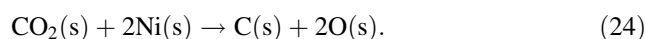
and with adsorbed oxygen (R21–R28),



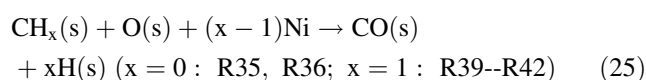
Decomposition of water (R29–R34).



and carbon dioxide (R35–R38),



Reaction of adsorbed species and production of CO and H₂



The reaction mechanism developed comprises the reactions of partial oxidation and steam reforming of methane and is based on the key reaction intermediate—adsorbed atomic oxygen O(s), that is the common intermediate for these reactions, indicated by TPR and in situ isotope transient experiments [31].

The unity bond index-quadratic exponential potential (UBI-QEP) approach [45–47] has been used to determine the heats of adsorption of adsorbed species, reaction enthalpy changes, and the activation barriers for all relevant steps of the mechanism. Both available experimental data and data derived from UBI-QEP calculations are used in the mechanism; the individual references are listed in Table 1. For the most part, the UBI-QEP calculations have been performed for empty surfaces, and, as a consequence, the mechanistic deductions drawn are strictly valid in the limit of zero adsorbate coverage, but nevertheless such deductions are in good agreement with experimental observations made under conditions of finite coverage [46]. Thus, the barrier of 57.7 kJ/mol for methane activation on Ni(111) surface via dissociation to CH₃ and H surface species used in the model is in good agreement with experiments, that give activation energies for CH₄ dissociation from thermal experiments in the range of 52–59 kJ/mol [48–50] for the Ni(111), (100), and (110) surfaces. Actually, the direct comparison of the activation barrier used in our mechanism for this reaction with barriers derived from ab initio calculations is sophisticated,

Table 1 Surface reaction mechanism (thermodynamic-non-consistent version)

Reaction	A ^a (cm, mol, s)	E _a (kJ/mol)	β (–)	References
R1 H ₂ + 2Ni(s) → 2H(s)	1.000 × 10 ^{−2}	0.0	0.0	[66], s.c. ^c
R2 O ₂ + 2Ni(s) → 2O(s)	1.000 × 10 ^{−2f}	0.0	0.0	[18], s.c. ^c
R3 CH ₄ + Ni(s) → CH ₄ (s)	8.000 × 10 ^{−3}	0.0	0.0	s.c. ^{c,g}
R4 H ₂ O + Ni(s) → H ₂ O(s)	1.000 × 10 ^{−1f}	0.0	0.0	[18], s.c. ^c
R5 CO ₂ + Ni(s) → CO ₂ (s)	1.000 × 10 ^{−5}	0.0	0.0	s.c. ^{c,g}
R6 CO + Ni(s) → CO(s)	5.000 × 10 ^{−1d}	0.0	0.0	[67, 68], s.c. ^c
R7 2H(s) → 2Ni(s) + H ₂	3.000 × 10 ⁺²¹	98.0	0.0	[31, 69]
R8 2O(s) → 2Ni(s) + O ₂	1.300 × 10 ⁺²²	464.0	0.0	[45]
R9 H ₂ O(s) → H ₂ O + Ni(s)	6.000 × 10 ⁺¹³	68.9	0.0	[45]
R10 CO(s) → CO + Ni(s)	1.000 × 10 ⁺¹³	122.4 − 50θ _{CO(s)} ^e	0.0	[66]
R11 CO ₂ (s) → CO ₂ + Ni(s)	1.000 × 10 ⁺⁰⁸	27.3	0.0	[45, 68]
R12 CH ₄ (s) → CH ₄ + Ni(s)	2.000 × 10 ⁺¹⁴	25.1	0.0	[47, 67]
R13 CH ₄ (s) + Ni(s) → CH ₃ (s) + H(s)	3.700 × 10 ⁺²¹	57.7	0.0	[47]
R14 CH ₃ (s) + H(s) → CH ₄ (s) + Ni(s)	3.700 × 10 ⁺²¹	56.1	0.0	[47]
R15 CH ₃ (s) + Ni(s) → CH ₂ (s) + H(s)	3.700 × 10 ⁺²⁴	100.0	0.0	[47]
R16 CH ₂ (s) + H(s) → CH ₃ (s) + Ni(s)	3.700 × 10 ⁺²¹	49.8	0.0	[47]
R17 CH ₂ (s) + Ni(s) → CH(s) + H(s)	3.700 × 10 ⁺²⁴	97.1	0.0	[47]
R18 CH(s) + H(s) → CH ₂ (s) + Ni(s)	3.700 × 10 ⁺²⁴	73.6	0.0	[47]
R19 CH(s) + Ni(s) → C(s) + H(s)	3.700 × 10 ⁺²¹	18.8	0.0	[47]
R20 C(s) + H(s) → CH(s) + Ni(s)	3.700 × 10 ⁺²¹	173.6	0.0	[47]
R21 CH ₄ (s) + O(s) → CH ₃ (s) + OH(s)	1.700 × 10 ⁺²⁴	88.3	0.0	This work
R22 CH ₃ (s) + OH(s) → CH ₄ (s) + O(s)	3.700 × 10 ⁺²¹	23.4	0.0	This work
R23 CH ₃ (s) + O(s) → CH ₂ (s) + OH(s)	3.700 × 10 ⁺²⁴	130.1	0.0	[46]
R24 CH ₂ (s) + OH(s) → CH ₃ (s) + O(s)	3.700 × 10 ⁺²¹	16.7	0.0	[46]
R25 CH ₂ (s) + O(s) → CH(s) + OH(s)	3.700 × 10 ⁺²⁴	126.8	0.0	[46]
R26 CH(s) + OH(s) → CH ₂ (s) + O(s)	3.700 × 10 ⁺²¹	40.2	0.0	[46]
R27 CH(s) + O(s) → C(s) + OH(s)	3.700 × 10 ⁺²¹	48.1	0.0	[59]
R28 C(s) + OH(s) → CH(s) + O(s)	3.700 × 10 ⁺²¹	139.7	0.0	[59]
R29 H(s) + O(s) → OH(s) + Ni(s)	5.000 × 10 ⁺²²	97.9	0.0	[45]
R30 OH(s) + Ni(s) → H(s) + O(s)	3.000 × 10 ⁺²⁰	34.3	0.0	[45]
R31 H(s) + OH(s) → H ₂ O(s) + Ni(s)	3.000 × 10 ⁺²⁰	42.7	0.0	[46]
R32 H ₂ O(s) + Ni(s) → H(s) + OH(s)	3.000 × 10 ⁺²²	87.0	0.0	[46]
R33 OH(s) + OH(s) → H ₂ O(s) + O(s)	3.000 × 10 ⁺²¹	100.0 ^g	0.0	This work
R34 H ₂ O(s) + O(s) → OH(s) + OH(s)	3.000 × 10 ⁺²¹	207.5 ^g	0.0	This work
R35 C(s) + O(s) → CO(s) + Ni(s)	5.200 × 10 ⁺²³	148.1	0.0	[47]
R36 CO(s) + Ni(s) → C(s) + O(s)	2.500 × 10 ⁺²¹	139.7 − 50θ _{CO(s)} ^e	−3.0 ^g	[47]
R37 CO(s) + O(s) → CO ₂ (s) + Ni(s)	3.000 × 10 ⁺¹⁹	123.6 − 50θ _{CO(s)} ^{e,g}	0.0	This work
R38 CO ₂ (s) + Ni(s) → CO(s) + O(s)	3.000 × 10 ⁺²³	88.0 ^g	−1.0 ^g	This work
R39 CO(s) + H(s) → HCO(s) + Ni(s)	5.000 × 10 ⁺¹⁹	96.2	−1.0 ^g	[45]
R40 HCO(s) + Ni(s) → CO(s) + H(s)	3.700 × 10 ⁺²¹	0.0 + 50θ _{CO(s)} ^e	0.0	[45]
R41 HCO(s) + Ni(s) → CH(s) + O(s)	3.700 × 10 ⁺²⁴	95.8	−3.0 ^g	[46]
R42 CH(s) + O(s) → HCO(s) + Ni(s)	3.700 × 10 ⁺²¹	146.0	0.0	[46]

^a The nominal value of the preexponential factor of an elementary reaction was assumed to be: 10¹³ N_A/Γ (cm²/mol, s), where N_A is Avogadro's number; 10¹³ (s^{−1}) is the order of magnitude of $\frac{k_B T}{h}$ (k_B the Boltzmann's constant, h Planck's constant) and would be the value expected from transition state theory; Γ = 1.5 × 10¹⁵ (site/cm²) is the site density, that was calculated by assuming a site area of 6.5 × 10^{−2} nm² as observed for nickel [1]

^b The reference indicates the source for the sticking coefficient or the activation energy

^c Initial sticking coefficient

^d Literature value without temperature dependence of initial sticking coefficient

^e Coverage dependence applies due to thermodynamic constraints

^f Value for Rh(111)

^g Estimated in this work based on the comparison of simulation and experiment

because in our model the methane molecule is assumed to exist in an adsorbed precursor state before dissociation to CH₃(s) and H(s). In ab initio calculations, usually direct dissociation of methane from the gas phase is considered; it is noted that the values reported in literature differ

significantly. Yang et al. [51] reported DFT results on the chemisorption of H and CH_x and the dissociative chemisorption of CH₄ on a Ni(111) surface using an embedded cluster CI approach. The activation energy calculated for CH₄ to CH₃ is 71 kJ/mol. Kratzer et al. [52] performed

DFT calculations on a Ni(111) slab to characterize the transition state for CH₄ dissociation. For the clean Ni surface a barrier of 109 kJ/mol was found. Bengaard et al. [26] used DFT to study methane steam reforming and graphite formation on Ni catalysts. The authors presented a complete potential energy diagram and estimate an activation barrier for the first methane activation step to be less than 91 kJ/mol; whereas Henkelman et al. reported 75 kJ/mol [53]. Recently, Blaylock et al. [35] investigated the thermochemistry and kinetics of steam methane reforming on Ni(111) using plane wave density functional theory and gave the barrier of dissociative adsorption of CH₄(g) to be 129 kJ/mol.

For the activation barrier of dehydrogenation of CH₃(s) to form CH₂(s) surface species we have used an UBI-QEP derived estimation of 100 kJ/mol, that is in good agreement with DFT calculations on Ni(111) proposing a barrier of 100 kJ/mol [54, 55]. UBI-QEP calculations lead to 146 kJ/mol for the activation barrier of HCO(s) production from CH(s) and O(s) and 0–50 kJ/mol for HCO(s) dehydrogenation into CO(s) and H(s); DFT calculations [31] proposed 151 and 20 kJ/mol, respectively.

Sticking coefficients are used as kinetic data for the adsorption of reactants and products (H₂, O₂, CH₄, H₂O, CO, CO₂) represented in the reaction mechanism. The mechanism of methane activation without oxygen is supported by HREEL and molecular beam investigations of methane decomposition on Ni(111) [56] and isotopic transient and steady-state experiments [31]. In the case of partial oxidation, the oxygen-assisted dissociation represents a further pathway for methane activation. Solymosi et al. [57] have observed that the addition of CO₂ to CH₄ in partial oxidation reaction greatly promoted the dissociation of CH₄. They assumed that the activation of CH₄ was facilitated by adsorbed oxygen generated in the decomposition of CO₂ or water. The implementation of the surface oxygenated specie HCO(s) in the mechanism is supported by TPSR and TR-FTIR experiments [58] and theoretical calculations with UBI-QEP method [45, 59]. Furthermore, DFT calculations of Wang et al. [33] and Pistonesi et al. [60] conclude that HCO species dissociation in CO and H fragments is a favorable reaction in steam reforming of methane on Ni(111).

4.2 Thermodynamic Consistency

The equilibrium of a chemical reaction,



is completely defined by the thermodynamic properties of the participating species. Expressed in terms of the

equilibrium constant, K_{pk} , the equilibrium activities, a_i^{eq} , obey the equation

$$K_{pk} = \prod_i (a_i^{\text{eq}})^{v_{ik}} = \exp\left(-\frac{\Delta_k G^0}{RT}\right). \quad (27)$$

The symbols are the stoichiometric coefficient $v_{ik} = v''_{ik} - v'_{ik}$, the gas constant R , the temperature T , and the change of free enthalpy at normal pressure p^0

$$\Delta_k G^0 = \sum_i v_{ik} G_i^0(T). \quad (28)$$

In case of gases, the activities can be approximated by their partial pressures $a_i = p_i/p^0$, and in case of surface species by their coverages $a_i = \theta_i$. When the dependence of the heat capacities on temperature is given by a forth-order polynomial [47] and standard enthalpies and entropies of formation, then the standard free enthalpies can be expressed in terms of seven coefficients, $a_{0,i}, \dots, a_{6,i}$:

$$G_i^0(T) = a_{0,i} + a_{1,i}T + a_{2,i}T^2 + a_{3,i}T^3 + a_{4,i}T^4 + a_{5,i}T^5 + a_{6,i}T \ln T. \quad (29)$$

In order to predict the correct equilibrium, the rate coefficients for the forward and the reverse reaction must obey the equation

$$\frac{k_{fk}}{k_{rk}} = K_{pk} \prod_i (c_i^0)^{v_{ik}}. \quad (30)$$

The c_i^0 are reference concentrations at normal pressure, i.e. $c_i^0 = p^0/RT$ for gas-phase species and $c_i^0 = \Gamma/\sigma_i$ for surface species.

However, one problem in setting up a reaction mechanism is the difficulty to define the thermodynamic data for intermediate surface species. Therefore, Eq. 30 cannot be used to calculate the rate coefficient of the reverse reaction. The forward and the reverse reaction are then defined separately with their own rate laws. Nevertheless, these rates cannot be chosen independently.

Assume an initial guess for a surface reaction mechanism. The rate coefficients for forward and reverse reactions may have been adjusted separately. Suppose that the thermodynamic data for species 1... N_u are unknown. For each pair of reversible reactions we can calculate an equilibrium constant using Eq. 30 and, according to Eq. 27, its logarithm yields the change of free enthalpy. (Note: coverage dependent activation energies are not considered at this stage.) Separation of the known and the unknown variables in Eq. 28 leads to

$$\Delta_k G^0 = \sum_{i=1}^{N_u} v_{ik} \tilde{G}_i^0(T) + \sum_{i=N_u+1}^N v_{ik} G_i^0(T), \quad (31)$$

that is a linear equation system for the unknown free enthalpies \tilde{G}_i^0 . Since most species are involved in more than one reaction, this system is usually over-determined. Inserting Eq. 29 for several temperatures T_j gives a system of linear equations in the unknown coefficients $\tilde{a}_{l,i}$:

$$\sum_{i=1}^{N_u} \sum_{l=0}^6 v_{ik} t_{lj} \tilde{a}_{l,i} = g_{kj} \quad \text{for all } k \text{ and } j, \quad (32)$$

where the following abbreviation have been used

$$g_{kj} = \Delta_k G^0(T_j) - \sum_{i=N_u+1}^N v_{ik} G_i^0(T_j) \quad (33)$$

and

$$t_{lj} = \begin{cases} T_j^l & \text{if } l < 6 \\ T_j \ln T_j & \text{if } l = 6 \end{cases} \quad (34)$$

An “optimal” set of parameters $\tilde{a}_{l,i}$ is determined by a weighted least-square approximation. The weights can be chosen individually for each pair of reactions according to a sensitivity analysis of the reaction mechanism. This guarantees that the equilibrium of crucial reaction steps will be shifted less than others after adjustment.

The newly adjusted thermodynamic coefficients are then used to calculate the change of free enthalpy for each reaction (31), the equilibrium constant (27), and the rate coefficient of the reverse reaction (30). In case the reverse reaction shall be expressed in terms of Arrhenius coefficients, another least square approximation using the rate constants at the discrete temperatures, T_j , is performed.

Since we prefer to write surface reaction mechanisms as pairs of irreversible reactions, this procedure has to be repeated during mechanism development after modification of rate coefficients belonging to any of these pairs.

Figure 2 illustrates the algorithm. The difference between this method and the scheme proposed by Mhadeshwar et al. [61] is the fact that in our procedure is no need to select a linearly independent set of reactions. Instead of distinguishing reactions between linear base and linear combinations, all reactions are treated equally by solving the same linear problem using a least-square fit.

The algorithm ensures thermodynamic consistency in a sense that the thermodynamic equilibrium of the participating gas-phase species is matched for a range of temperatures, while writing all reversible reactions as pairs of independent forward and backward reactions. Thus, the thermodynamic data of the intermediate species is not needed for the evaluation of the reaction rates. Due to the assumptions of the mean-field model, this data shall not be considered thermodynamic properties of a well-defined binding state of a given molecule.

The thermodynamically consistent surface reaction mechanism that was established on base of the “source” surface reaction mechanism (Table 1) using the adjustment algorithm for the temperature interval 500–2000 K is given in Table 2. The associated thermodynamic data of all species is temperature dependent. As an example, the resulting specific enthalpies at 500 and 2000 K are given in Table 3.

5 Results and Discussion

The developed detailed multi-step heterogeneous reaction mechanism presented in Table 2 matches the kinetic data for steam reforming on Ni catalyst well. Figures 3, 4, 5, 6 and 7 show a good agreement between the calculated and experimental conversion, selectivity, and yield of products

Fig. 2 Illustration of the adjustment algorithm to set up thermodynamically consistent surface reaction mechanisms

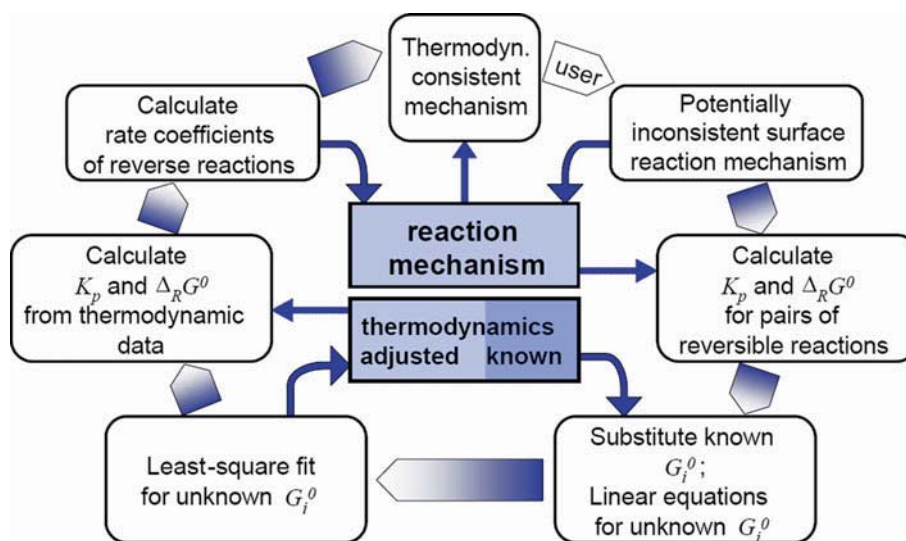


Table 2 Thermodynamically consistent surface reaction mechanism, electronic version available from www.detchem.com

	Reaction	A (cm, mol, s)	E _a (kJ/mol)	β (-)
R1	H ₂ + 2Ni(s) → 2H(s)	1.000 × 10 ⁻⁰²	s.c.	0.0
R2	2H(s) → 2Ni(s) + H ₂	2.545 × 10 ⁺¹⁹	81.21	0.0
R3	O ₂ + 2 Ni(s) → 2O(s)	1.000 × 10 ⁻⁰²	s.c.	0.0
R4	2O(s) → 2Ni(s) + O ₂	4.283 × 10 ⁺²³	474.95	0.0
R5	CH ₄ + Ni(s) → CH ₄ (s)	8.000 × 10 ⁻⁰³	s.c.	0.0
R6	CH ₄ (s) → CH ₄ + Ni(s)	8.705 × 10 ⁺¹⁵	37.55	0.0
R7	H ₂ O + Ni(s) → H ₂ O(s)	1.000 × 10 ⁻⁰¹	s.c.	0.0
R8	H ₂ O(s) → H ₂ O + Ni(s)	3.732 × 10 ⁺¹²	60.79	0.0
R9	CO ₂ + Ni(s) → CO ₂ (s)	1.000 × 10 ⁻⁰⁵	s.c.	0.0
R10	CO ₂ (s) → CO ₂ + Ni(s)	6.447 × 10 ⁺⁰⁷	25.98	0.0
R11	CO + Ni(s) → CO(s)	5.000 × 10 ⁻⁰¹	s.c.	0.0
R12	CO(s) → CO + Ni(s)	3.563 × 10 ⁺¹¹	111.27 - 50θ _{CO(s)}	0.0
R13	CH ₄ (s) + Ni(s) → CH ₃ (s) + H(s)	3.700 × 10 ⁺²¹	57.7	0.0
R14	CH ₃ (s) + H(s) → CH ₄ (s) + Ni(s)	6.034 × 10 ⁺²¹	61.58	0.0
R15	CH ₃ (s) + Ni(s) → CH ₂ (s) + H(s)	3.700 × 10 ⁺²⁴	100.0	0.0
R16	CH ₂ (s) + H(s) → CH ₃ (s) + Ni(s)	1.293 × 10 ⁺²³	55.33	0.0
R17	CH ₂ (s) + Ni(s) → CH(s) + H(s)	3.700 × 10 ⁺²⁴	97.10	0.0
R18	CH(s) + H(s) → CH ₂ (s) + Ni(s)	4.089 × 10 ⁺²⁴	79.18	0.0
R19	CH(s) + Ni(s) → C(s) + H(s)	3.700 × 10 ⁺²¹	18.8	0.0
R20	C(s) + H(s) → CH(s) + Ni(s)	4.562 × 10 ⁺²²	161.11	0.0
R21	CH ₄ (s) + O(s) → CH ₃ (s) + OH(s)	1.700 × 10 ⁺²⁴	88.3	0.0
R22	CH ₃ (s) + OH(s) → CH ₄ (s) + O(s)	9.876 × 10 ⁺²²	30.37	0.0
R23	CH ₃ (s) + O(s) → CH ₂ (s) + OH(s)	3.700 × 10 ⁺²⁴	130.1	0.0
R24	CH ₂ (s) + OH(s) → CH ₃ (s) + O(s)	4.607 × 10 ⁺²¹	23.62	0.0
R25	CH ₂ (s) + O(s) → CH(s) + OH(s)	3.700 × 10 ⁺²⁴	126.8	0.0
R26	CH(s) + OH(s) → CH ₂ (s) + O(s)	1.457 × 10 ⁺²³	47.07	0.0
R27	CH(s) + O(s) → C(s) + OH(s)	3.700 × 10 ⁺²¹	48.1	0.0
R28	C(s) + OH(s) → CH(s) + O(s)	1.625 × 10 ⁺²¹	128.61	0.0
R29	H(s) + O(s) → OH(s) + Ni(s)	5.000 × 10 ⁺²²	97.9	0.0
R30	OH(s) + Ni(s) → H(s) + O(s)	1.781 × 10 ⁺²¹	36.09	0.0
R31	H(s) + OH(s) → H ₂ O(s) + Ni(s)	3.000 × 10 ⁺²⁰	42.7	0.0
R32	H ₂ O(s) + Ni(s) → H(s) + OH(s)	2.271 × 10 ⁺²¹	91.76	0.0
R33	OH(s) + OH(s) → H ₂ O(s) + O(s)	3.000 × 10 ⁺²¹	100.0	0.0
R34	H ₂ O(s) + O(s) → OH(s) + OH(s)	6.373 × 10 ⁺²³	210.86	0.0
R35	C(s) + O(s) → CO(s) + Ni(s)	5.200 × 10 ⁺²³	148.1	0.0
R36	CO(s) + Ni(s) → C(s) + O(s)	1.354 × 10 ⁺²²	116.12 - 50θ _{CO(s)}	-3.0
R37	CO(s) + O(s) → CO ₂ (s) + Ni(s)	2.000 × 10 ⁺¹⁹	123.6 - 50θ _{CO(s)}	0.0
R38	CO ₂ (s) + Ni(s) → CO(s) + O(s)	4.653 × 10 ⁺²³	89.32	-1.0
R39	CO(s) + H(s) → HCO(s) + Ni(s)	4.019 × 10 ⁺²⁰	132.23	-1.0
R40	HCO(s) + Ni(s) → CO(s) + H(s)	3.700 × 10 ⁺²¹	0.0 + 50θ _{CO(s)}	0.0
R41	HCO(s) + Ni(s) → CH(s) + O(s)	3.700 × 10 ⁺²⁴	95.8	-3.0
R42	CH(s) + O(s) → HCO(s) + Ni(s)	4.604 × 10 ⁺²⁰	109.97	0.0

during the steam reforming for all experimental conditions studied. Both experimentally measured and numerical predicted reveal that thermodynamic equilibrium is not reached at temperature below 1000 K (Figs. 3, 4, 6). The model predicts the experimentally determined H₂/CO ratio as a function of temperature reasonably well (Fig. 6), while

this ratio is higher compared to equilibrium calculation at temperature below 1000 K (Fig. 6). The slightly overprediction of the H₂/CO ratio with respect to the experimental measurements at the higher S/C ratios (Fig. 7d) is probably due to the underestimation of water–gas shift reaction in the model, especially at low temperature.

Table 3 Specific enthalpies of the given gas-phase species and adjusted values for surface species

	H (500 K) (kJ/mol)	H (2000 K) (kJ/mol)
H ₂	5.9	53.0
O ₂	6.1	59.2
CH ₄	-66.6	48.7
H ₂ O	-234.9	-169.0
CO	-104.6	-53.8
CO ₂	-385.2	-302.1
H(s)	-39.4	-15.0
O(s)	-234.5	-214.9
CH ₄ (s)	-104.6	-2.6
H ₂ O(s)	-299.5	-233.6
CO(s)	-218.7 + 50θ _{CO(s)}	-169.4 + 50θ _{CO(s)}
CO ₂ (s)	-414.0	-334.9
CH ₃ (s)	-68.4	5.5
CH ₂ (s)	16.4	62.1
CH(s)	74.4	92.1
C(s)	-28.6	35.8
OH(s)	-212.0	-167.6
HCO(s)	-131.7	-63.8

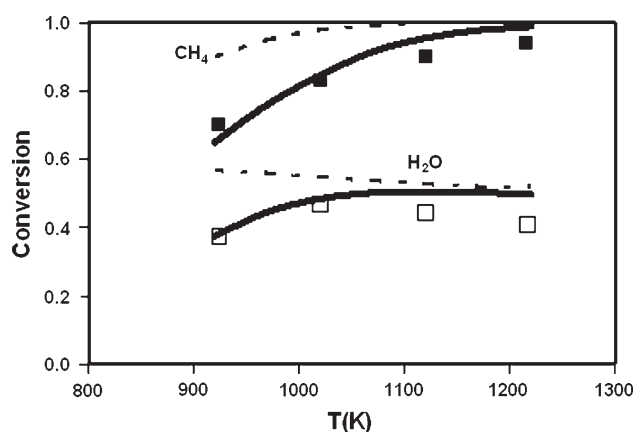


Fig. 3 Methane and water conversion as a function of temperature in methane steam reforming: S/C = 2.77, 75% Ar; scatter—experiment (filled symbols methane, empty symbols water), solid lines simulation, dash lines equilibrium calculation

Figure 7 shows the effect of inlet steam to carbon (S/C) ratio on methane conversion (a), water conversion (b), CO-selectivity (c), and H₂/CO-ratio (d) in methane steam reforming at 1020 K. The experiment and modeling data show that methane conversion increases and the CO selectivity decreases with increasing S/C. Methane conversion reaches 95% at S/Cs close to 4 and 1215 K (approximately 80% for S/C 2). CO selectivity ranges from 50% (S/C ~4) up to 78% (S/C 1.8). At medium temperatures (923 K) methane conversion is in the range of 75–55%, and the CO selectivity is between 13 and 27%.

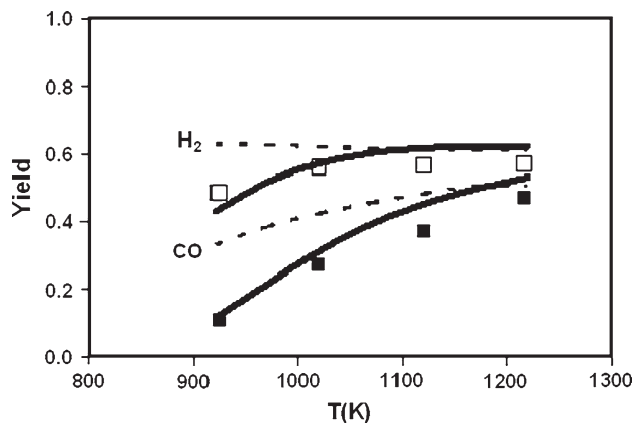


Fig. 4 H₂- and CO-yield as a function of temperature in methane steam reforming S/C = 2.77, 75% Ar; scatter—experiment (filled symbols CO, empty symbols H₂), solid lines simulation, dash lines equilibrium calculation

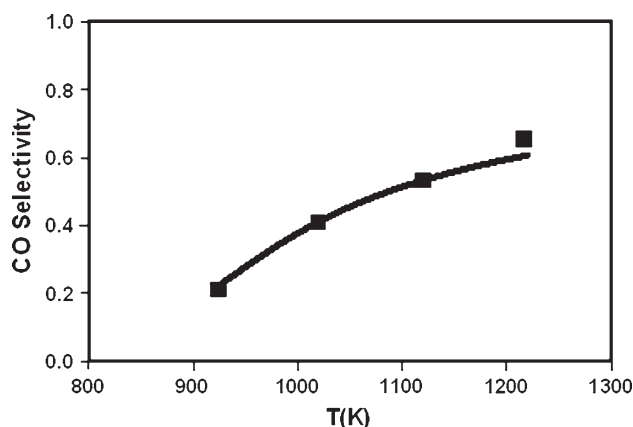


Fig. 5 Effect of temperature on CO-selectivity in methane steam reforming: S/C = 2.77, 75 % Ar. Symbols/lines represent the experimental/numerical data, respectively

The thermodynamic equilibrium in the reaction system (10)–(15) has to be considered to analyze the product composition. All these reactions are reversible at the wide range of temperature applied. Although the reversible reactions (10)–(12) are strongly endothermic and reactions (13)–(15) are exothermic, the over-all heat of reactions (10)–(15) may be positive, zero, or negative, depending on the process conditions.

At low steam to carbon ratios and low catalyst exit temperature (~900 K), the over-all heat of reactions (9)–(14) is positive. This is reflected by the low methane conversion and low CO-content in the product stream (Figs. 3, 4, 5, 6, 7). At high temperature, the over-all reaction becomes endothermic and methane conversion increases (Fig. 3, 7a), because at high temperature the equilibrium of both endothermic reactions, Eqs. 12 and 13, the shift reaction and the methanation reaction are

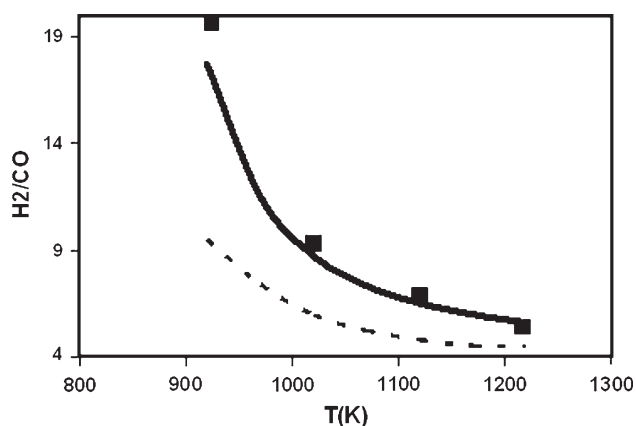


Fig. 6 Effect of temperature on H₂/CO-ratio in methane steam reforming: S/C = 2.77, 75% Ar; symbols experiment, solid line simulation, dash line equilibrium calculation

left-shifted leading to less methane and more carbon monoxide in the product stream. Furthermore, at high temperatures, the CO concentration increases, because of the equilibrium shift in the Boudouard reaction (15) to carbon monoxide, and CH₄ concentration decreases due to methane cracking (16). This is in agreement with trends of the thermodynamic equilibrium constants for reactions (9), (12), (15), and (16) at the temperature range of 273–1273 K [1].

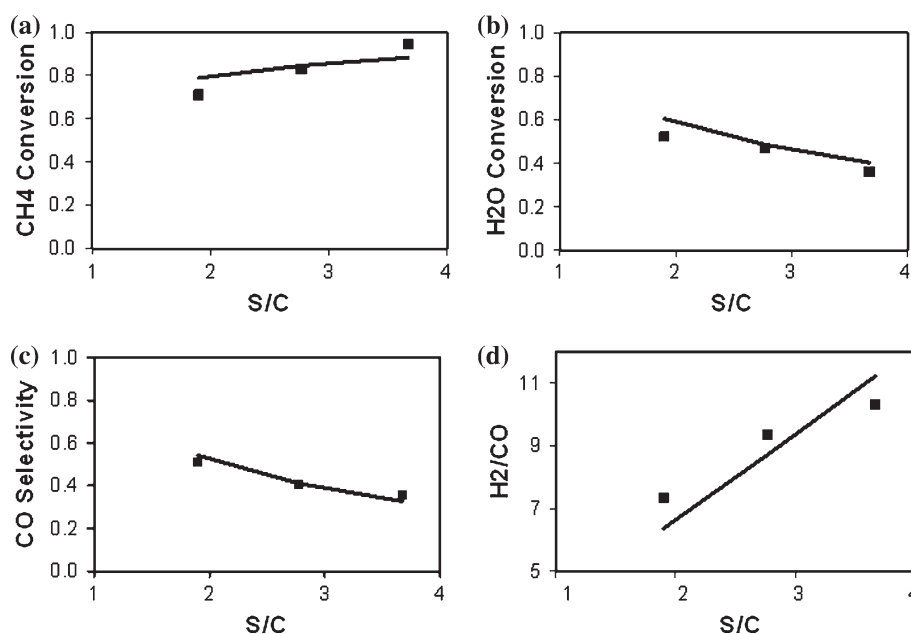
In agreement with Aparicio's conclusion [31] that the reforming rate is found to depend largely on the elementary reactions R35–R36 of the reaction mechanism, the equilibrium of this reversible reaction is strongly sensitive to the temperature deviation. Surface oxygen species involved in C–O bond formation can be produced via dissociative adsorption of oxygen R2 or adsorption and dissociation of

water R4, R32–R33, R29–R30. The availability of surface oxygen is assumed to play a key role in determining the rate of syngas formation at high temperature.

The model shows that the site coverage of C(s) is larger than the one of CH₄(s), CH₃(s), CH₂(s), CH(s), and HCO(s) (Fig. 8), which is in good agreement with the experimental results of Bradford and Vannice [15]. The reaction of CH(s) destruction (R19) has a much lower activation barrier than that of CH_x(s) (x = 2–4) dehydrogenation reaction R13, R15 and R17. This means that once a CH(s) species is formed, it immediately dehydrogenates to carbon and hydrogen. The model identifies that the elementary steps R19–R20, R27–R28 and R35–R36, involving carbon formation from methane and carbon monoxide, are important in determining the coverage of surface carbon species. Elementary steps of carbon formation from methane dehydrogenation are lower activated compared with CO dissociation. Therefore, the main part of surface carbon was assumed to be produced from methane, which is in agreement with the results of in situ isotope-labelled ¹³CO₂ transient experiments for mixed reforming [12] and DFT calculations [33]. Surface carbon C(s) is possibly nickel carbide as suggested by Kroll et al. [62] or it is just the adsorbed atomic carbon. Such carbon could well be a precursor of the graphitic carbon that causes deactivation. A detailed kinetic of deactivation was not considered in our model.

We performed a sensitivity analysis of the reaction mechanism at three temperatures: 920, 1020, and 1120 K with S/C = 1.9 (75% Ar). In particular, we analysed sensitivity of exit molar fraction of CH₄, CO, CO₂, H₂, and H₂O, by perturbing the pre-exponentials of each reaction. Results for the methane mole fraction, presented in Fig. 9,

Fig. 7 Effect of inlet steam to carbon (S/C) ratio on methane conversion (a); water conversion (b); CO-selectivity (c); H₂/CO-ratio (d) in steam reforming of methane, T = 1020 K, 75% Ar; symbols/lines represent the experimental/numerical data, respectively



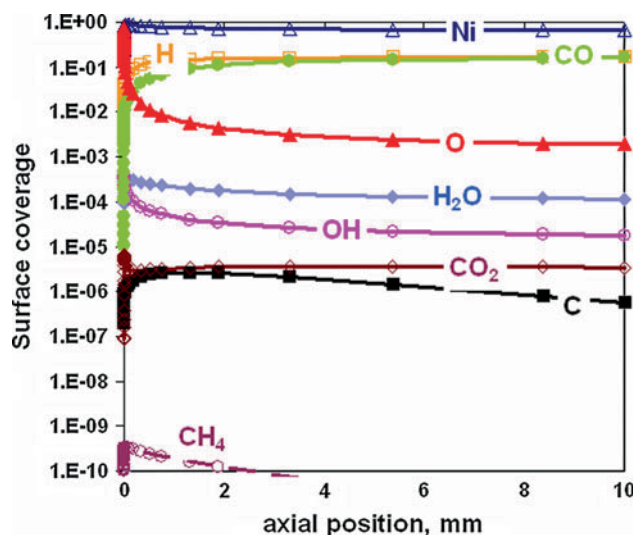


Fig. 8 Computed surface coverage of adsorbed species along the catalytic channel wall in methane steam reforming at 1120 K, $S/C = 2.77$

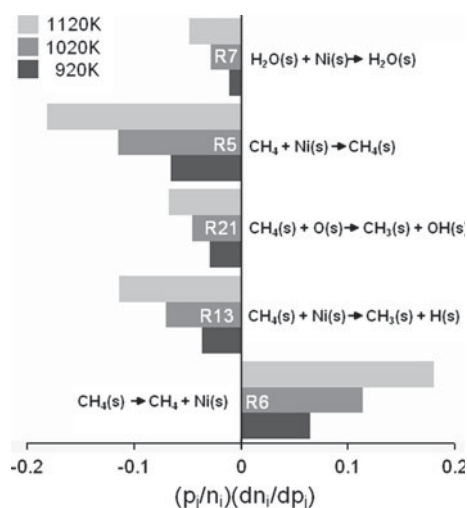


Fig. 9 Sensitivity coefficients for methane mole fraction as function of temperature for methane steam reforming, $S/C = 1.9$ (75% Ar). Only the most sensitive reactions are presented

show that the system was highly sensitive to the methane adsorption and further $CH_4(s)$ dehydrogenation steps (with and without oxygen assistance).

In order to further test the applicability of the heterogeneous surface reaction mechanism developed, experiments conducted by Ryu and Lee [63] were modeled. In their experiments, SR of CH_4 was studied over two reduced Ni catalyst wash-coated on metal monolith (21 wt% Ni on MgO and Al_2O_3), packed into a quartz tube reactor. The weight of the Ni catalyst used to make the washcoat was 3 g in 15.2 cm^3 ; the method to prepare the catalyst is explained in Refs. [63, 64]. The single monolith with a diameter of 2.2 cm being 2 cm in length consists of over

300 channels (640 cpsi) with an inner hydraulic diameter of 0.536 mm. As before, in the simulation only one channel was analyzed using the software DETCHEM^{CHANNEL}. The reactor was isothermally operated at atmospheric pressure at $S/C = 3$ without dilution. The inlet temperature was 700 K at a gas hourly space velocity (GHSV) of 9000 h^{-1} . As shown in Fig. 10, the heterogeneous reaction mechanism presented is also able to predict the experimental conversion of methane sufficiently well.

Meanwhile, the mechanism established on base of the “source” mechanism, developed in this work using the adjustment algorithm for temperature 1073 K has been used to model steam and DR of methane-containing fuels in Ni/YSZ anodes of Solid-Oxide Fuel Cells (SOFC) and was able to reproduce all experimentally observed trends [36, 65]. The applicability of the detailed reaction scheme to quite different systems reveals that the intrinsic kinetics of SR over Ni-based catalysts is not very strongly influenced by the support material and the external conditions applied; a feature of SR and DR of methane that further supports the general findings of Wei and Iglesia [30].

6 Conclusions

The kinetics of the steam reforming of methane over nickel coated monoliths has been experimentally studied in a flow reactor. A detailed multi-step heterogeneous reaction mechanism for steam and DR of methane as well as partial and total oxidation, including the reverse water–gas shift reaction, methanation, and carbon formation routes was developed. Kinetic parameters were estimated using semi-empirical UBI-QEP calculations as well as data from the here presented experiments and from literature. Modeling

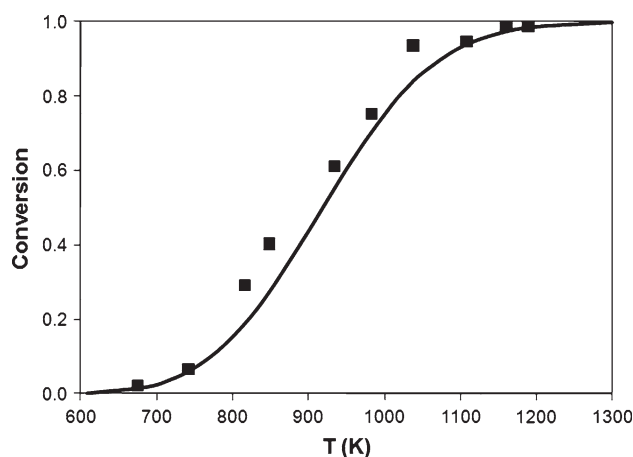


Fig. 10 Methane conversion as function of temperature over metal monolith washcoated with Ni catalyst, $S/C = 3$; experimental data taken from Ryu and Lee [63]; symbols/lines represent the experimental/numerical data, respectively

showed that the availability of surface oxygen plays a key role in determining the rate of synthesis gas formation in reforming processes.

Due to the problem that thermodynamic data for individual surface species are usually not available, a procedure has been derived and applied throughout the development process to ensure the over-all thermodynamic consistency of the mechanism. This approach can also be used to quickly adapt surface reaction rate parameters in a thermodynamically consistent way when a catalytic system is slightly changed, e.g. by modifications of supports and additives, as long as the general reaction features of the reaction mechanism are not altered.

Experimentally measured conversion and selectivity at strongly varying conditions were well-computed by numerical simulations using the developed reaction mechanism and adequate mass transport models. In particular, steam reforming over nickel-based catalysts was considered for varying temperature and steam/methane ratio taking experimental data not only from experiments presented here but also from literature.

Future work will focus on the application of the mechanism to partial and total oxidation as well as autothermal and DR conditions and on the implementation of a coking model into the surface reaction scheme.

References

1. Rostrup-Nielsen JR (1984) In: Anderson JR, Boudart M (eds) Catalytic steam reforming in catalysis—science and technology. Springer-Verlag, Berlin
2. Levent M, Gunn DJ, El Bousiffi MA (2003) *Int J Hydrogen Energy* 28:945
3. Michael BC, Donazzi A, Schmidt A (2009) *J Catal* 265:117
4. Trimm DL (1997) *Catal Today* 37:233
5. Yang Z, Zhang Y, Wang X (2010) *Energy Fuels* 24:785
6. Ochoa-Fernández E, Lacalle-Vilà C, Christensen KO, Walmsley JC, Rønninga M, Holmen A, Chen D (2007) *Top Catal* 45:3–8
7. Dissanayake D, Rosynek MP, Kharas KS, Lunsford JH (1991) *J Catal* 132:117
8. Vermeiren WJM, Blomsma E, Jacobs PA (1992) *J Catal* 13:427
9. Hannemann S, Grunwaldt JD, van Vegten N (2007) *Catal Today* 126:54
10. Hickman DA, Schmidt LD (1993) *AIChE J* 39:1164
11. Choudhary VR, Rajput AM, Rane VH (1992) *Catal Lett* 16:269
12. Qin D, Lapszewicz J, Jiang X (1996) *J Catal* 159:140
13. Gadalla AM, Sommer ME (1989) *Chem Eng Sci* 44:2825
14. Liu ZW, Roh HS, Jun KW (2003) *J Ind Eng Chem* 9:753
15. Bradford MCJ, Vannice MA (1996) *Appl Catal A* 142:97
16. Scognamiglio D, Russo L, Maffettone P (2009) *Ind Eng Chem Res* 48:1804
17. Schwiedernoch R, Tischer S, Correa C, Deutschmann O (2003) *Chem Eng Sci* 58:633
18. Deutschmann O, Schmidt L (1998) *AIChE J* 44:2465
19. Mhadeshwar AB, Vlachos DGJ (2005) *Phys Chem B* 109:16819
20. Deutschmann O, Schwiedernoch R, Maier L, Chatterjee D (2001) In: Iglesia E, Spivey JJ, Fleisch TH (eds) *Natural gas conversion* VI, vol 136. Studies in surface science and catalysis. Elsevier, Amsterdam
21. Quiceno R, Pérez-Ramírez J, Warnatz J, Deutschmann O (2006) *Appl Catal A* 303:166
22. Xu J, Froment GF (1989) *AIChE J* 35:88
23. Chen D, Lødeng R, Omdahl K, Anundskås A, Olsvik O, Holmen A (2001) *Stud Surf Sci Catal* 139:93
24. Rostrup-Nielsen JR, Hansen JHB (1993) *J Catal* 144:38
25. Rostrup-Nielsen JR, Christiansen LJ, Bak Hausen J-H (1988) *Appl Catal* 43:287
26. Bengaard HS, Nørskov JK, Sehested J, Clausen BS, Nielsen LP, Molenbroek AM, Rostrup-Nielsen JR (2002) *J Catal* 209:365
27. Hoang DL, Chan SH, Ding OL (2005) *Chem Eng J* 112:1
28. Mogensen D, Grunwaldt J-D, Hendriksen PV, Dam-Johansen K, Nielsen JU (2011) *J Power Sources* 196:25
29. Enger BC, Lødeng R, Holmen A (2008) *Appl Catal A* 346:1–27
30. Wei J, Iglesia E (2004) *J Catal* 224:370
31. Aparicio LM (1997) *J Catal* 165:262
32. Chen D, Lødeng R, Svendsen H, Holmen A (2011) *Ind Eng Chem Res* 50(5):2600
33. Wang S-G, Liao X-Y, Hu J, Cao D-B, Li Y-W, Wang J, Jiao H (2007) *Surf Sci* 601:1271
34. Wang S-G, Cao D-B, Li Y-W, Wang J, Jiao H (2006) *J Phys Chem B* 110:9976
35. Blaylock DW, Ogura T, Green WH, Beran GJO (2009) *J Phys Chem C* 113:4898
36. Hecht E, Gupta GK, Zhu H, Dean AM, Kee RJ, Maier L, Deutschmann O (2005) *Appl Catal A* 295:40
37. Janardhanan VM, Deutschmann O (2006) *J Power Sources* 162:1192
38. Schädel BT, Deutschmann O (2007) In: Noronha FB, Schmal M, Sousa-Aguiar EF (eds) *Natural gas conversion VIII*, vol 167. Studies in surface science and catalysis. Elsevier, Amsterdam, p 207
39. Schädel BT, Duisberg M, Deutschmann O (2009) *Catal Today* 142:42
40. Raja LL, Kee RJ, Deutschmann O, Warnatz J, Schmidt LD (2000) *Catal Today* 59:47
41. Coltrin ME, Kee RJ, Rupley FM (1990) SURFACE CHEMKIN, version 4.0, a Fortran package for analyzing heterogeneous chemical kinetics at a solid-surface–gas-phase interface. Sandia National Laboratories report, SAND90-8003B
42. Deutschmann O (2008) In: Ertl G, Knözinger H, Schüth F, Weitkamp J (eds) *Computational fluid dynamics simulation of catalytic reactors*. Handbook of heterogeneous catalysis, 2nd edn. Wiley-VCH, Weinheim
43. Deutschmann O, Tischer S, Kleditzsch S, Janardhanan VM, Correa C, Chatterjee D, Mladenov N, Minh HD (2008) DETCHEM™ Software package, 2.2 edn. Karlsruhe. www.detchem.com.
44. Tischer S, Deutschmann O (2005) *Catal Today* 105:407
45. Shustorovich E (1990) *Adv Catal* 37:101
46. Shustorovich E, Sellers H (1998) *Surf Sci Rep* 31:5
47. Bell AT (1991) In: Shustorovich E (ed) *Metal surface reaction energetics: theory and application to heterogeneous catalysis, chemisorption and surface diffusion*. Wiley-VCH, Weinheim
48. Beebe TP Jr, Goodman DW, Kay BD, Yates JT Jr (1987) *J Chem Phys* 87:2305
49. Chorkendorff I, Alstrup I, Ullmann S (1990) *Surf Sci* 227:291
50. Nielsen BØ, Luntz AC, Holmblad PM, Chorkendorff I (1995) *Catal Lett* 32:15
51. Yang H, Whitten JL (1992) *J Chem Phys* 96:5529
52. Kratzer P, Hammer B, Nørskov JK (1996) *J Chem Phys* 105:5595
53. Henkelman G, Arnaldsson A, Jonsson H (2006) *J Chem Phys* 124:4706
54. Michaelides A, Hu P (2000) *J Chem Phys* 112:6006
55. Michaelides A, Hu P (2000) *J Chem Phys* 112:8120

56. Ceyer ST, Yang QY, Lee MB, Beckeler JD, Johnson AD (1993) In: Bibby DH, Chang CD, Howe RF, Yurchak S (eds) Methane conversion. Elsevier, Amsterdam
57. Erdohelyi A, Cserenyi J, Solymosi F (1993) *J Catal* 141:287
58. Yan Q, Wu T, Yang L, Luo C, Weng W, Chao Z, Wan H (2000) *J Nat Gas Chem* 9:1
59. Hei MJ, Chen HB, Yi J, Lin YJ, Lin YZ, Wie G, Liao DW (1998) *Surf Sci* 417:82
60. Pistonesi C, Juan A, Irigoyen B, Amadeo N (2007) *Appl Surf Sci* 253:4427
61. Mhadeshwar AB, Wang H, Vlachos DGJ (2003) *Phys Chem B* 107:12721
62. Kroll VCH, Swaan HM, Mirodatos C (1996) *J Catal* 161:409
63. Ryu J-H, Lee KY (2007) *J Power Sources* 171:499
64. Heon J, Yoon WL (2003) *J Power Sources* 124:76
65. Zhu H, Kee RJ, Janardhanan VM, Deutschmann O, Goodwin DG (2005) *J Electrochem Soc* 152:A2427
66. Christmann K (1991) In: Baumgärtel H, Franck EU, Grünbein W (eds) Topics in physical chemistry, vol 1. Steinkopf Verlag, Darmstadt
67. Brass SG, Ehrlich G (1987) *Surf Sci* 187:21
68. Matsushima T (1983) *Surf Sci* 127:403
69. Christmann K, Schöber O, Ertl G, Neumann M (1974) *J Chem Phys* 60:4528